Electronic Supplementary Material (ESI) for ChemComm.

Red Phosphorus Encapsulated in 3D N-Doped Porous Carbon Nanofibers: An Enhanced Sodium-Ion Battery Anode Material

Experimental section

1 Chemicals

All chemicals, obtained from commercial suppliers, were utilized without any further purification process. BC pellicles, containing approximately 1% (vol/vol) fiber content, were procured from Hainan Yeguo Foods Co., Ltd, Hainan, China. Urea (AR) was sourced from Sinopharm Chemical Reagent Co. LTD, and red phosphorus was acquired from Sigma-Aldrich.

2 Material Preparation

In order to synthesize 3D N-doped porous carbon nanofibers (N-PCNFs), we first immersed the BC hydrogels in a 0.1 M urea solution and stirred for three days. This was followed by freeze-drying to yield the desired BC/urea hybrid aerogels. Afterward, the hybrid aerogels were subjected to pyrolysis under a N_2 atmosphere at 800 °C for 2 h with a heating rate of 10 °C min^{-1}.

For the synthesis of free-standing N-PCNFs embedded with red P (RP@N-PCNFs), we employed a vaporization-condensation strategy to infiltrate RP into the N-PCNFs. Typically, a total of 0.1 g of RP and 0.1 g of as-prepared N-PCNFs were put into an ampoule and sealed them after vacuum extraction. The mixture is then annealed at 600 ° C for 8 h to generate the steam necessary for the diffusion of P into the pores to achieve their full mixing. To convert white P into RP, the sample was subjected to treatment at 260 °C for 24 h. Finally, the product was washed with CS_2 to remove any residual white P, followed by vacuum drying at 60 °C to obtain the RP@N-PCNFs.

3 Structural Characterizations

TEM was carried out using a Hitachi H7700 transmission electron microscope with a charge-coupled device imaging system and an accelerating voltage of 100 kV. HRTEM was performed on JEOL-2100F with an acceleration voltage of 200 kV. STEM-EDS element mapping was carried out on a JEOL-2100F equipped with an Oxford INCA

system. X-ray diffraction (XRD) data were recorded on a Japan Rigaku Ultima IV X-ray diffractometer equipped with Cu Kα radiation (λ = 1.54056 Å). Thermogravimetric analysis (TGA) was measured by a TGA Q5000IR analyzer under O_2 flow with a temperature ramp of 10 °C min^{-1}. X-ray photoelectron spectroscopy (XPS) was acquired on an X-ray photoelectron spectrometer (ESCALAB MKII) with an excitation source of Mg K_α radiation (1253.6 eV). N_2 adsorption-desorption analysis was conducted using an ASAP 2020 Accelerated Surface Area and Porosimetry instrument (Micromeritics), equipped with an automated surface area, at 77 K using BET calculations for the surface area. The pore size distribution plot was recorded from the adsorption branch of the isotherm based on the Barrett-Joyner-Halenda model.

4 Electrochemical Measurements

To investigate the electrochemical performance of RP@N-PCNFs composite, the CR2032 coin cells were assembled with the RP@N-PCNFs composite as the working electrode and Na metal (purity ≥ 99.5%, SCRC) as counter and reference electrode. The electrode size is about 1 cm^2 and the areal mass is about 2 mg cm^{-2}. The assembly of the half-cells took place inside a glove box (MBRAUN LABMASTER 130) filled with high purity Ar atmosphere (O_2 and H_2O < 0.1 ppm). The electrolyte consisted of 1 M $NaClO_4$, ethylene carbonate (EC), and dimethyl carbonate (1:1, w/w), with 1% volume of fluoroethylene carbonate as the additives. A glass fiber separator from Whatman was selected due to the large sodium ion radius. To characterize the galvanostatic charge-discharge properties, the battery test system (Neware BTS-610) was employed. The capacity was calculated based on the mass of the composite.

5 Density functional theory simulation

First-principal calculations were conducted using Density Functional Theory (DFT). We utilized the Generalized Gradient Approximation (GGA) in conjunction with the Perdew-Burke-Ernzerhof function[1] to account for electron exchange corrections. The plane-wave expansion of the Projector Augmented Waves (PAWs) was capped at an energy cutoff of 520 eV. We established convergence criteria for energy and force at 10^{-5} eV and 0.02 eV/Å, respectively. To accurately depict the dispersion interaction, we applied Grimme's DFT-D3[2] correlation. A vacuum layer approximately 25 Å thick

was introduced in the vertical direction to preclude interactions between adjacent layers. For structural relaxation, the Brillouin zone was sampled using the Monkhorst-Pack scheme with a 2×1×1 k-point mesh in the Gamma-centered grids.

6 Finite element method

The finite element simulations of volumetric strain and stress distribution in free P and RP@N-PCNFs after sodiation were performed via COMSOL Multiphysics 5.6. The multiphysics interface of hygroscopic swelling was applied to simulate the sodiation process, which couples the modulus of Solid Mechanics and Transport of Diluted Species. The equations of hygroscopic swelling can be described as the following equations: $\varepsilon_{hs} = \beta_h M_k C_k$, $F_{inel}^{-1} \rightarrow F_{hs}^{-1} F_{inel}^{-1}$, $F_{hs} = I + \varepsilon_{hs}$. In this simulation process, the relative expansion coefficient (β_h) is 5.6×10^{-4} m^3/kg. And the Young's modulus of Na_3P and C is 26 GPa and 20 GPa, respectively.

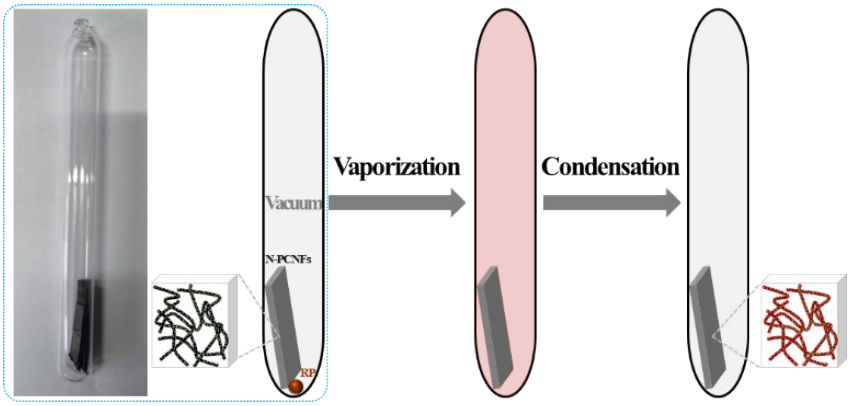

Figure S1. Schematic illustration of the vaporization-condensation process.

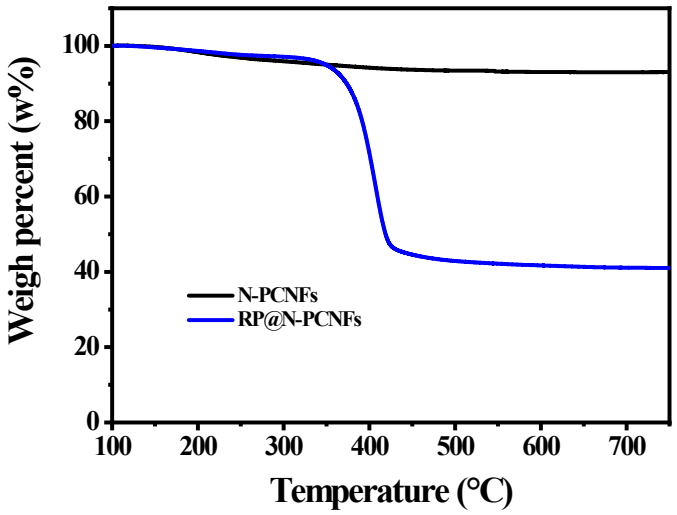

Figure S2. Thermogravimetric curves for RP@N-PCNFs and N-PCNFs.

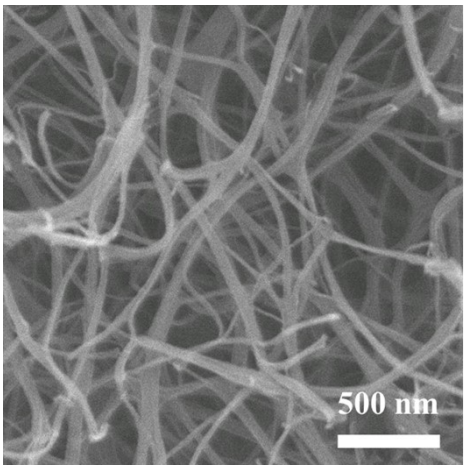

Figure S3. SEM image of the N-PCNFs.

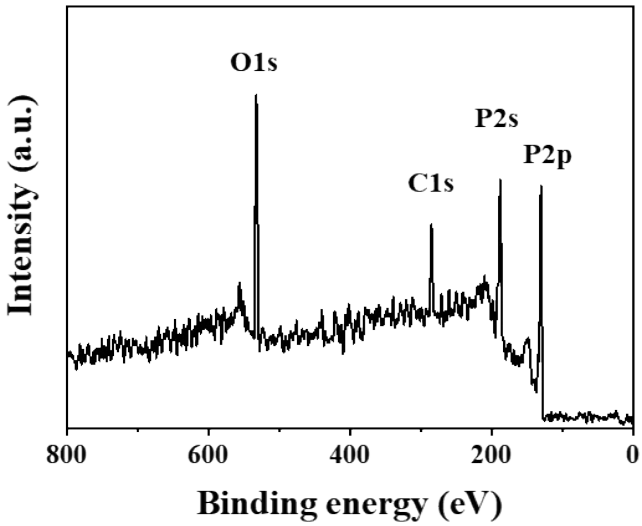

Figure S4. Global XPS profile of RP@N-PCNFs.

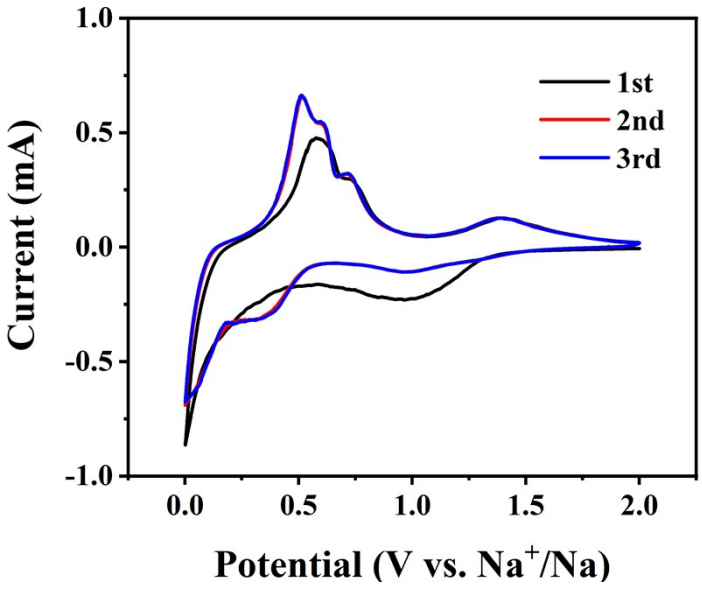

Figure S5. Cyclic voltammetry curves of the RP@N-PCNFs electrode.

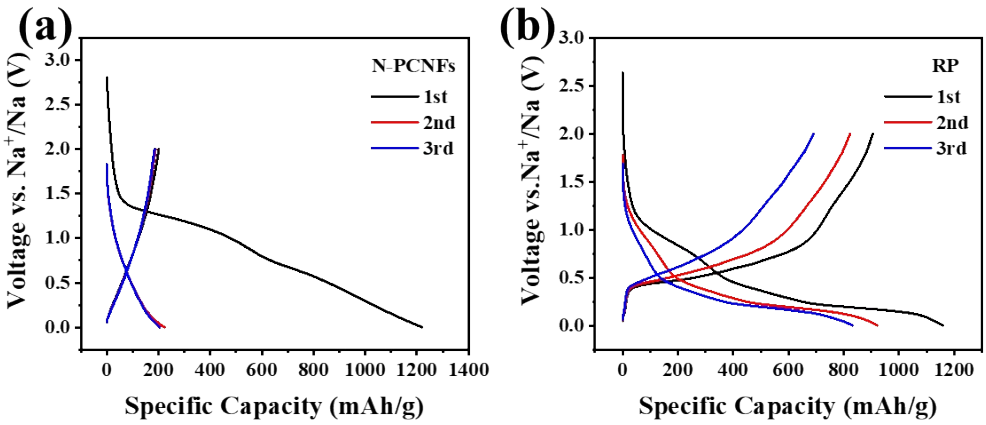

Figure S6. Initial three cycle charge/discharge profiles of (a) N-PCNFs and (b) RP anodes at 0.1 A g^{-1}.

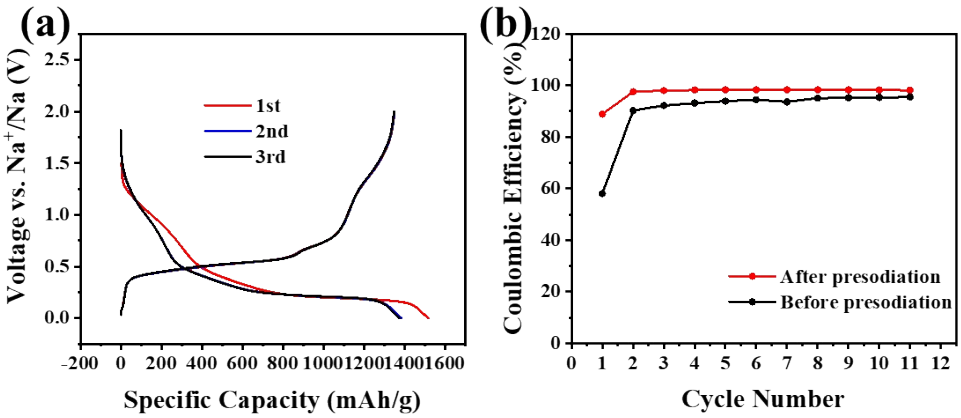

Figure S7. (a) Initial three cycle charge/discharge profiles of the RP@N-PCNFs after presodiation at 0.1 A g^{-1}. (b) The CE of RP@N-PCNFs before and after presodiation.

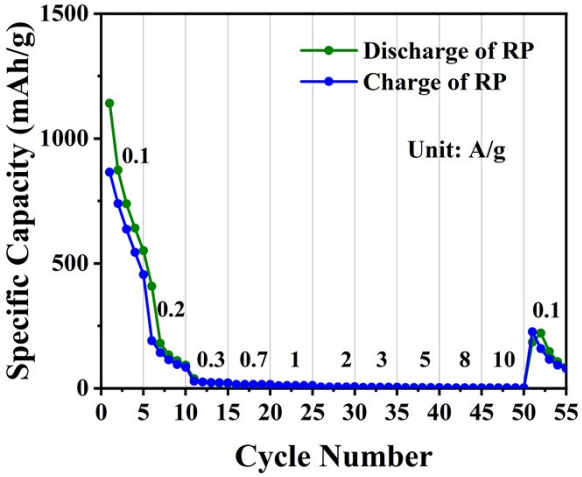

Figure S8. Rate capability of RP anode at different current densities.

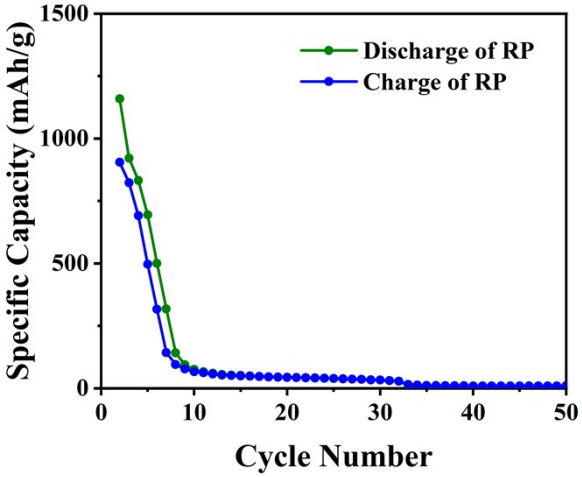

Figure S9. Cycling performance of RP anode at 0.1 A g^{-1}.

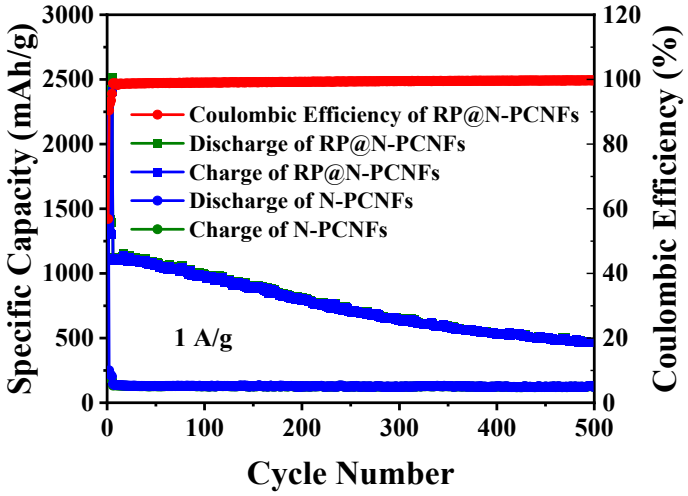

Figure S10. Cycling performance of the RP@N-PCNFs and N-PCNFs anodes at 1 A g^{-1}.

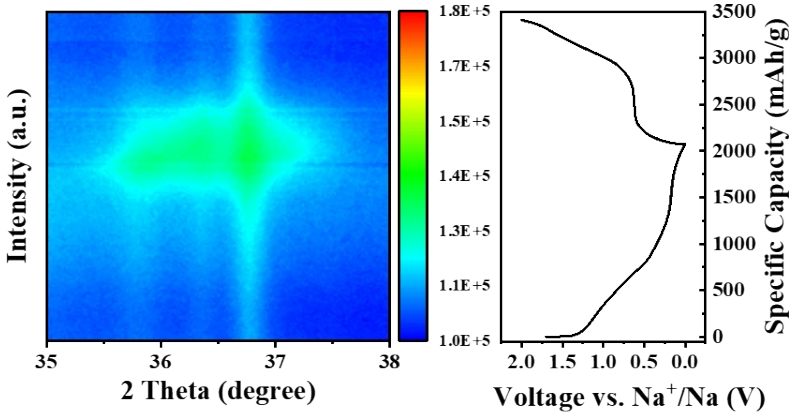

Figure S11. In situ XRD patterns of RP@N-PCNFs during the initial discharge/charge process and corresponding charge/discharge profiles.

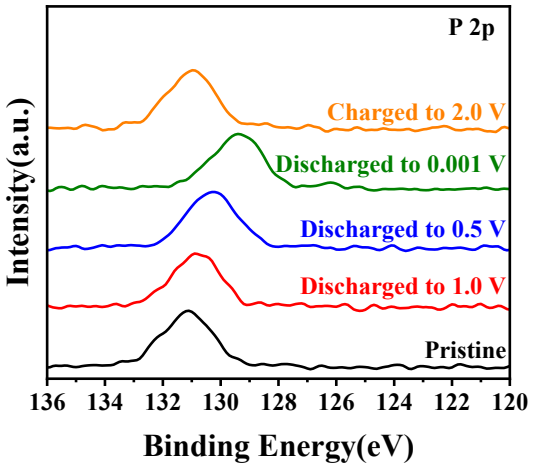

Figure S12. Ex situ P 2p XPS for RP@N-PCNFs electrodes at different states.

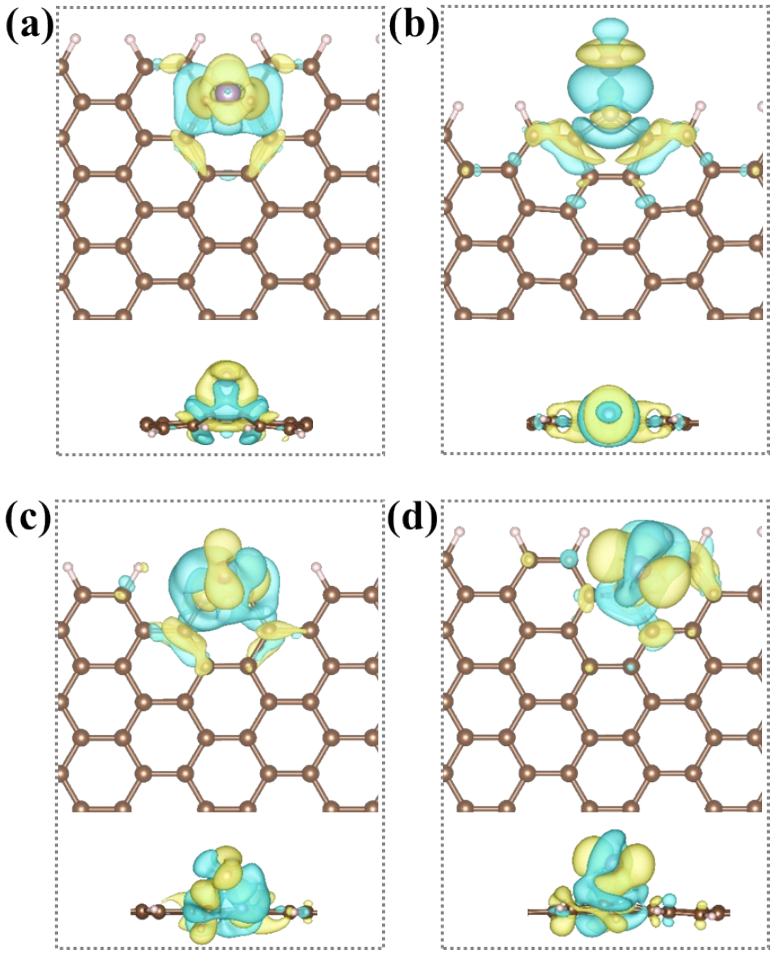

Figure S13. Electron density differences of a single P atom absorbed in (a) CNFs and (b-d) N-PCNFs structures. Blue and yellow domains represent depleted electrons and accumulated electrons, respectively.

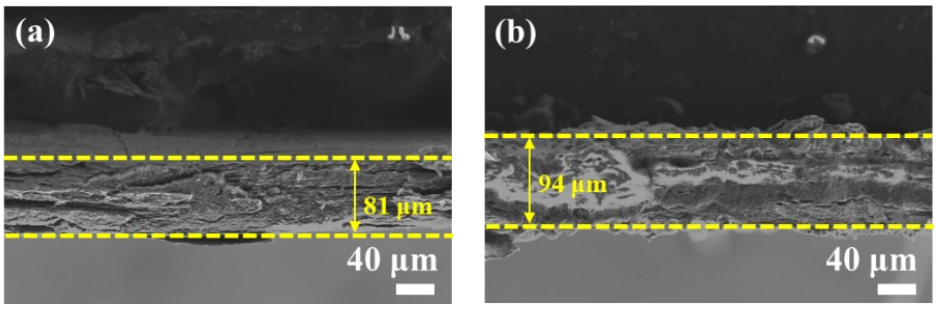

Figure S14. The SEM images of the cross section of RP@N-PCNFs electrode (a) before and (b) after alloying with Na.

Table S1. Specific surface areas and pore volume of N-PCNFs and RP@N-PCNFs.

Sample	Specific surface area (m^2 g^{-1})	Pore volume (cm^3 g^{-1})
N-PCNFs	355	0.656
RP@N-PCNFs	12	0.035

Table S2. Electrochemical performance of RP/C composite anode materials for SIBs in recent five years.

Electrode materials	Current density (A g^{-1})[§]	Specific capacity (mAh g^{-1})[#]	Cycling performance (Capacity retention)	Refrence
pNa-P/C@S	0.1	891.7	-	[3]
	0.2	887.0	98%@100 cycles	
	0.5	871.1	-	
	1.0	824.7	-	
	2.5	766.7	-	
WDC/CNTs@RP I	0.52	2069.6	-	[4]
	1.3	1504.8	-	
	2.6	1059.3	60%@700 cycles	
	5.2	783.2	-	
	7.8	574.7	-	
	10.4	313.3	-	
	13	179.5	-	
P@NGCA	0.2	786	68.4%@100 cycles	[5]
	0.4	725	-	
	0.6	643	-	
	0.8	581	-	
	1.0	508	-	
	2.0	417	-	
RP/SWCNTs	0.125	1720	-	[6]
	0.625	1230	-	
	1.25	872	-	
	2.5	465	99.5%@280 cycles	
	5.0	304	-	
	6.25	254	-	
RP@CNCs	0.1	1514	90%@150 cycles	[7]
	0.5	1100	-	
	1.0	980	-	
	2.0	840	-	
	5.0	610	80%@1300 cycles	
RP/rGA	0.1	1974	71%@20 cycles	[8]

P_2@N-SGCNT	0.1	744	93%@500 cycles	[9]
	0.2	671	-	
	0.5	621	-	
	1.0	579	-	
	2.0	531	-	
P_{red}@CNF	0.1	862	75.6%@522 cycles	[10]
	0.2	711	84.7%@991 cycles	
	0.5	686	69.4%@2284 cycles	
	1.0	532	67%@5000 cycles	
NRP-rGO	0.1	1157	70%@100 cycles	[11]
	2.0	516	86%@1400 cycles	
	5.0	391	66%@5000 cycles	
RH-3-1-RP/CS	1.0	478	-	[12]
	2.0	435	-	
	4.0	375	97.5%@2000 cycles	
	6.0	321	-	
	8.0	290	-	
rP@N-BC	0.05	1319	-	[13]
	0.1	1148	-	
	5	454	-	
PC@RP	0.1	667	87%@100 cycles	[14]
	0.3	630	-	
	0.5	596	89%@300 cycles	
	2.0	434	-	
HPCNS-P	0.1	608	80%@300 cycles	[15]
	0.2	475	-	
	0.5	373	-	
	1.0	304	76%@1000 cycles	
	2.0	192	-	
P@C-GO/MOF-5	0.1	1095	-	[16]
	0.5	970	-	
	2.0	839	93%@100 cycles	
	5.0	697	-	
	8.0	555	-	
P/CFs/RGO	0.05	943.1	75.7%@55 cycles	[17]
	0.1	850.6	-	
	0.2	779.2	-	
	0.4	694.1	-	
	0.6	634.7	-	
	0.8	585.2	-	
	1.0	521.2	-	
P–CNT@PD	0.26	1175	-	[18]
	0.52	962	-	
	1.3	709	-	

	2.6	599	80%@2000 cycles	
	5.2	486	64%@5000 cycles	
HNPRP[‖]	0.26	2023.3	-	[19]
	0.52	1833.2	-	
	1.3	1498.5	-	
	2.6	1164.7	74%@1000 cycles	
	5.2	759.6	-	
HPC/P1	0.26	822	-	[20]
	0.52	785	-	
	1.3	708	76.6%@100 cycles	
	2.6	533	-	
	5.2	353	-	
P@TBMC-2.4	0.05	1050	-	[21]
	0.2	1000	-	
	0.5	940	-	
	1.0	810	-	
	2.0	650	-	
	4.0	550	-	
	6.0	480	-	
	8.0	430	-	

Note: [§]Current density was calculated based on the mass of composites. [#]Specific capacity was calculated based on the mass composites. [‖]Current density and specific capacity were calculated based on the mass of RP.

References

[1] J.P. Perdew, K. Burke, M. Ernzerhof, Generalized Gradient Approximation Made Simple, Physical Review Letters, 77 (1996) 3865-3868.

[2] S. Grimme, J. Antony, S. Ehrlich, H. Krieg, A consistent and accurate ab initio parametrization of density functional dispersion correction (DFT-D) for the 94 elements H-Pu, JOURNAL OF CHEMICAL PHYSICS, 132 (2010).

[3] J. Song, M. Wu, K. Fang, T. Tian, R. Wang, H. Tang, NaF-rich interphase and high initial coulombic efficiency of red phosphorus anode for sodium-ion batteries by chemical presodiation, J. Colloid Interface Sci., 630 (2023) 443-452.

[4] Z. Zhu, Z. Pei, B. Liu, D. Sun, Y. Fang, X. Lei, X. Liu, S. Niu, H. Pan, J. Zhou, Y. Qian, G. Wang, Hierarchical Ion/Electron Networks Enable Efficient Red Phosphorus Anode with High Mass Loading for Sodium Ion Batteries, Advanced

Functional Materials, 32 (2022).

[5] Y. Sun, Q. Wu, K. Zhang, Y. Liu, X. Liang, H. Xiang, A high areal capacity sodium-ion battery anode enabled by a free-standing red phosphorus@N-doped graphene/CNTs aerogel, Chem. Commun., 58 (2022) 7120-7123.

[6] H. Kaur, B. Konkena, C. Gabbett, R. Smith, M. McCrystall, R. Tian, A. Roy, T. Carey, V. Vega-Mayoral, V. Nicolosi, J.N. Coleman, Amorphous 2D-Nanoplatelets of Red Phosphorus Obtained by Liquid-Phase Exfoliation Yield High Areal Capacity Na-Ion Battery Anodes, Adv. Energy Mater., 13 (2023) 2203013.

[7] W. Liu, L. Du, S. Ju, X. Cheng, Q. Wu, Z. Hu, X. Yu, Encapsulation of Red Phosphorus in Carbon Nanocages with Ultrahigh Content for High-Capacity and Long Cycle Life Sodium-Ion Batteries, ACS Nano, 15 (2021) 5679-5688.

[8] Y. Yan, S. Xia, H. Sun, Y. Pang, J. Yang, S. Zheng, A promising 3D crystalline red P/reduced graphene oxide aerogel architecture anode for sodium-ion batteries, Chemical Engineering Journal, 393 (2020).

[9] J. Ruan, F. Mo, Z. Long, Y. Song, F. Fang, D. Sun, S. Zheng, Tailor-Made Gives the Best Fits: Superior Na/K-Ion Storage Performance in Exclusively Confined Red Phosphorus System, ACS Nano, 14 (2020) 12222-12233.

[10] Y. Liu, Q. Liu, C. Jian, D. Cui, M. Chen, Z. Li, T. Li, T. Nilges, K. He, Z. Jia, C. Zhou, Red-phosphorus-impregnated carbon nanofibers for sodium-ion batteries and liquefaction of red phosphorus, Nat. Commun., 11 (2020) 2520.

[11] W. Liu, S. Ju, X. Yu, Phosphorus-Amine-Based Synthesis of Nanoscale Red Phosphorus for Application to Sodium-Ion Batteries, ACS Nano, 14 (2020) 974-984.

[12] H. Jin, H. Lu, W. Wu, S. Chen, T. Liu, X. Bi, W. Xie, X. Chen, K. Yang, J. Li, A. Liu, Y. Lei, J. Wang, S. Wang, J. Lu, Tailoring conductive networks within hollow carbon nanospheres to host phosphorus for advanced sodium ion batteries, Nano Energy, 70 (2020) 104569.

[13] W. Tian, L. Wang, K. Huo, X. He, Red phosphorus filled biomass carbon as high-capacity and long-life anode for sodium-ion batteries, J. Power Sources, 430

(2019) 60-66.

[14] J. Cheng, G. Zhang, P. Wang, C.Y. Wang, Y.X. Yin, Y.K. Li, F.F. Cao, Y.G. Guo, Confined Red Phosphorus in Edible Fungus Slag-Derived Porous Carbon as an Improved Anode Material in Sodium-Ion Batteries, ACS Appl. Mater. Interfaces, 11 (2019) 47948-47955.

[15] S. Yao, J. Cui, J. Huang, J.-Q. Huang, W.G. Chong, L. Qin, Y.-W. Mai, J.-K. Kim, Rational Assembly of Hollow Microporous Carbon Spheres as P Hosts for Long-Life Sodium-Ion Batteries, Adv. Energy Mater., 8 (2018) 1702267.

[16] Y. Wu, Z. Liu, X. Zhong, X. Cheng, Z. Fan, Y. Yu, Amorphous Red Phosphorus Embedded in Sandwiched Porous Carbon Enabling Superior Sodium Storage Performances, Small, 14 (2018) 1703472.

[17] X. Ma, L. Chen, X. Ren, G. Hou, L. Chen, L. Zhang, B. Liu, Q. Ai, L. Zhang, P. Si, J. Lou, J. Feng, L. Ci, High-performance red phosphorus/carbon nanofibers/graphene free-standing paper anode for sodium ion batteries, J. Mater. Chem. A, 6 (2018) 1574-1581.

[18] W. Liu, X. Yuan, X. Yu, A core-shell structure of polydopamine-coated phosphorus-carbon nanotube composite for high-performance sodium-ion batteries, Nanoscale, 10 (2018) 16675-16682.

[19] S. Liu, H. Xu, X. Bian, J. Feng, J. Liu, Y. Yang, C. Yuan, Y. An, R. Fan, L. Ci, Hollow nanoporous red phosphorus as an advanced anode for sodium-ion batteries, Journal of Materials Chemistry A, 6 (2018) 12992-12998.

[20] M. Li, N. Feng, M. Liu, Z. Cong, J. Sun, C. Du, Q. Liu, X. Pu, W. Hu, Hierarchically porous carbon/red phosphorus composite for high-capacity sodium-ion battery anode, Sci. Bull., 63 (2018) 982-989.

[21] D. Liu, X. Huang, D. Qu, D. Zheng, G. Wang, J. Harris, J. Si, T. Ding, J. Chen, D. Qu, Confined phosphorus in carbon nanotube-backboned mesoporous carbon as superior anode material for sodium/potassium-ion batteries, Nano Energy, 52 (2018) 1-10.